

Meminductor synaptic coupling in a heterogeneous HR-FHN neuron network: Model, dynamics, and DSP implementation

Yang Yin(尹扬) and Zhijun Li(李志军)

Citation: Chin. Phys. B, 2026, 35 (**6**): 060503. DOI: 10.1088/1674-1056/ae56e2
http://cpb.iphy.ac.cn; http://iopscience.iop.org/cpb

What follows is a list of articles you may be interested in

Spiking-bursting alternating chaos mediated by a locally active memristor

Yuxia Li(李玉霞), Xintong Yue(岳新同), Hui Chang(常辉), Baoxing Han(韩宝兴), and Yan Zhang(张燕)
Chin. Phys. B, 2026, 35 (**3**): 030504. DOI: 10.1088/1674-1056/ae44f9

Dynamics analysis and DSP implementation of the Rulkov neuron model with memristive synaptic crosstalk

Yichen Bi(毕毅晨), Jun Mou(牟俊), Herbert Ho-Ching Iu, Nanrun Zhou(周南润), Santo Banerjee, and Suo Gao(高锁)
Chin. Phys. B, 2026, 35 (**1**): 010504. DOI: 10.1088/1674-1056/ae1728

Energy adaptive regulation of a multifunctional neuron circuit

Xi-Kui Hu(胡锡奎), Juan Yang(杨娟), and Ping Zhou(周平)
Chin. Phys. B, 2026, 35 (**1**): 010503. DOI: 10.1088/1674-1056/ae1451

Dynamics and synchronization of neural models with memristive membranes under energy coupling

Jingyue Wan(万婧玥), Fuqiang Wu(吴富强), Jun Ma(马军), and Wenshuai Wang(汪文帅)
Chin. Phys. B, 2024, 33 (**5**): 050504. DOI: 10.1088/1674-1056/ad1dcc

A flux-controlled model of meminductor and its application in chaotic oscillator

Guang-Yi Wang(王光义), Pei-Pei Jin(靳培培), Xiao-Wei Wang(王晓炜), Yi-Ran Shen(沈怡然), Fang Yuan(袁方), Xiao-Yuan Wang(王晓媛)
Chin. Phys. B, 2016, 25 (**9**): 090502. DOI: 10.1088/1674-1056/25/9/090502

SPECIAL TOPIC — Biophysical circuits: Modeling & applications in neuroscience

Meminductor synaptic coupling in a heterogeneous HR–FHN neuron network: Model, dynamics, and DSP implementation

Yang Yin(尹扬) and Zhijun Li(李志军)[†]

School of Automation and Electronic Information, Xiangtan University, Xiangtan 411105, *China*

(Received 15 January 2026; revised manuscript received 20 March 2026; accepted manuscript online 25 March 2026)

To functionally emulate the history-dependent plasticity and electromagnetic induction effects inherent in biochemical synapses, this paper proposes a heterogeneous neural network model in which Hindmarsh–Rose (HR) neurons and FitzHugh–Nagumo (FHN) neurons are coupled via a synaptic connection composed of a meminductor in series with a resistor. This architecture explicitly decouples synaptic function: the linear resistor models the instantaneous conductive pathway, while the meminductor implements the history-dependent plastic pathway. The complex firing dynamics of the coupled system are systematically investigated through bifurcation diagrams, Lyapunov exponent spectra, phase portraits, and time-series analysis. The results show that variations in synaptic coupling strength and coupling resistance can induce transitions between diverse firing patterns, including chaotic spiking, periodic bursting, and alternations between periodic and chaotic states. Crucially, the meminductive synapse introduces activity-dependent multistability, manifested as the coexistence of multiple firing patterns determined by its initial internal state. Phase synchronization analysis further demonstrates that adjusting the coupling resistance provides an independent control mechanism that effectively enhances or suppresses synchronous firing between the two heterogeneous neurons, even at a fixed coupling strength. Finally, the physical feasibility of the system is validated through successful digital implementation on a digital signal processor (DSP) platform, as experimental measurements show excellent agreement with numerical simulations. This study establishes the meminductor as a biomimetically grounded element for chemical synapse emulation and provides a dynamically rich, hardware-validated platform for neuromorphic computing and information processing.

Keywords: meminductor, heterogeneous neuron network, firing pattern, synchronization, DSP implementation

PACS: 05.45.–a, 87.19.lg, 87.19.lj, 87.19.lm

DOI: 10.1088/1674-1056/ae56e2 **CSTR:** 32038.14.CPB.ae56e2

1. Introduction

In 1971, Professor Chua theoretically postulated the memristor as the fourth fundamental circuit component.[1] This hypothesis was subsequently validated in 2008 when researchers at Hewlett–Packard (HP) Labs successfully fabricated a physical memristor, sparking extensive worldwide research interest.[2,3] Following this breakthrough, Di Ventura *et al.* expanded the family of memory devices by introducing the memcapacitor and meminductor as memristive derivatives.[4] Due to their inherent nonlinearity, these memory devices have demonstrated substantial potential for applications across diverse fields, including computer memory, programmable analog circuits, chaotic circuits, and neural systems.

Within the realm of neuromorphic engineering, accurately emulating biological neural systems remains a paramount challenge. As the fundamental units of the nervous system, neurons are responsible for sensing, processing, and transmitting information via electrochemical signals known as action potentials.[5] These signals underpin higher cognitive functions, with neural communication occurring through either electrical or chemical synapses.[6–9] Electrical synapses, realized via gap junctions, facilitate direct, bidirectional communication with fast ionic coupling between neurons. Chemical synapses, by contrast, involve a more complex unidirectional process wherein presynaptic neurotransmitter release modulates postsynaptic ion channels. This mechanism enables sophisticated signal processing while exhibiting profound short- and long-term plasticity — widely regarded as the cornerstone of learning and memory.[7,10]

While memristors have been widely employed to emulate resistive coupling in electrical synapses,[11–13] increasing attention has been directed toward electromagnetic effects in neural dynamics. For instance, Qin *et al.* introduced a memristive chain Hopfield neural network using a flux-controlled memristor to model electromagnetic induction, revealing rich coexisting dynamical behaviors with hardware validation.[14] Boya *et al.* further demonstrated that electromagnetic radiation can significantly reshape Hopfield network dynamics, inducing antimonotonicity, bursting oscillations, and multiscroll attractors.[15] In addition, Yang *et al.* developed a memristive neuron model incorporating flux-controlled and inductive ele-

[†]Corresponding author. E-mail: lizhijun@xtu.edu.cn

© 2026 Chinese Physical Society and IOP Publishing Ltd. All rights, including for text and data mining, AI training, and similar technologies, are reserved.

ments, showing that external acoustic and magnetic fields can effectively modulate neuronal firing patterns.[16] These studies underscore the non-negligible role of electromagnetic factors in shaping neural activity. From a biophysical perspective, chemical synaptic transmission involves neurotransmitter release and ionic flux, both accompanied by transient electromagnetic phenomena.[17,18] This suggests that modeling synaptic interaction solely through resistive memory elements may be insufficient to capture potential induction-related modulation effects.

Motivated by the inductive characteristics of chemical synapses, numerous studies have introduced inductive coupling into neural and chaotic systems. Inspired by the physical properties of inductive coils, Yao *et al.* proposed a magnetic-field coupling scheme to synchronize neurons with different firing modes, demonstrating stable synchronization in scale-free networks.[19] Liu *et al.* constructed an equivalent Josephson junction model incorporating an inductive coil, systematically analyzing the dynamical effects of combined inductive and memristive interactions.[20] Li *et al.* employed a parallel inductor–capacitor coupling channel to connect two memristive Chua circuits, showing that optimal LC matching enhances synchronization.[21] Ma *et al.* further demonstrated that appropriate inductor coupling facilitates synchronization and suppresses chaotic oscillations in coupled Chua circuits.[22] Traditional linear inductors, however, lack the nonlinear memory essential for modeling synaptic adaptation, highlighting a critical gap in available hardware analogs.

Chemical synapses are fundamental to neural information processing, characterized by both instantaneous signal transfer and adaptive, activity-dependent modulation. This dual functionality, however, poses significant challenges for emulation using conventional circuit elements such as resistive memristors.[23,24] While memristors emulate certain resistive switching behaviors, they fail to account for the inductive aspects inherent in synaptic dynamics, underscoring a fundamental limitation in existing neural models.

This limitation has motivated the exploration of higher-order memory devices, whose intrinsic nonlinearity and state–history dependence offer a promising pathway toward bioinspired synaptic modeling.[25–28] Among these, the meminductor stands out as a particularly compelling candidate. Defined by an inductance that depends on its historical magnetic flux,[4] the meminductor inherently embodies both nonlinearity and memory. Its state-dependent inductive behavior and internal flux memory naturally capture synaptic efficacy that evolves with prior activity, providing a functional analogy to biological mechanisms such as residual calcium accumulation underlying short-term plasticity (STP).[29]

Although recent studies have integrated memory elements into neural models, most have focused on memristive or memcapacitive mechanisms,[30–32] overlooking the inductive aspects critical for fully capturing synaptic plasticity and history-dependent dynamics. The explicit use of a meminductor as the core coupling element in a heterogeneous neural network — particularly within a topology designed to decompose synaptic function into instantaneous conductive and history-dependent plastic pathways — remains largely unexplored. This gap presents a distinct opportunity to enhance both the biological fidelity and functional richness of hardware-based neural emulation.

To address this, we propose a novel heterogeneous neuron network in which a Hindmarsh–Rose (HR) neuron and a FitzHugh–Nagumo (FHN) neuron are coupled via a meminductor–resistor series synapse. This architecture offers a functional hardware analog of a chemical synapse by explicitly separating its operation into two complementary aspects: (i) a linear resistor modeling the instantaneous, ohmic conduction pathway, and (ii) a meminductor modeling the history-dependent, plastic pathway. The meminductor's state variable evolves with past neuronal activity, implementing a form of short-term synaptic plasticity that modulates efficacy based on recent spiking history. We hypothesize that this design will yield not only biomimetically plausible dynamics but also rich, controllable nonlinear behaviors that are valuable for neuromorphic computing.

The main innovations and contributions of this work are summarized as follows. (i) We propose a novel heterogeneous HR–FHN neuron network coupled through a meminductor–resistor series synapse, offering a functional decomposition approach to modeling chemical synaptic coupling. (ii) We systematically investigate the effects of coupling strength and resistance on firing patterns and synchronization, demonstrating that the meminductive synapse enables activity-dependent multistability and flexible phase synchronization control. (iii) We experimentally validate the physical realizability and operational stability of the proposed model on a digital signal processor (DSP) platform, confirming the feasibility of implementing meminductor-based synapses in practical neuromorphic hardware.

The rest of this paper is organized as follows. Section 2 introduces the mathematical model of the meminductor and the coupled HR–FHN neuron system, followed by an equilibrium point analysis. Section 3 details the complex dynamical behaviors of the system, examining the influences of coupling parameters and initial conditions, along with a phase synchronization analysis. Section 4 presents the DSP-based hardware implementation. Conclusions are provided in the final section.

2. Meminductor-based HR–FHN neuron model

2.1. Model of the meminductor

To emulate synaptic connections between neurons, a flux-controlled meminductor is proposed and defined as

$$\begin{cases} i = (a + b\rho^2)\varphi, \\ \dfrac{\mathrm{d}\rho}{\mathrm{d}t} = k\varphi - k_1\rho + k_2 v, \\ \dfrac{\mathrm{d}\varphi}{\mathrm{d}t} = v, \end{cases} \tag{1}$$

where i denotes the meminductor's current, v represents the voltage across the meminductor, ϕ is the flux across the meminductor, and ρ is an internal state variable. The parameters a, b, k, k_1, and k_2 govern the nonlinear characteristics of the meminductor. The corresponding inverse meminductance is given by

$$L^{-1}(\rho) = (a + b\rho^2). \tag{2}$$

To validate the meminductor characteristics, a sinusoidal current signal $I = I_S \cos(\omega t)$ is applied to it. When the frequency is fixed at $\omega = 0.1$ and the amplitude I_S is sampled at 0.1, 0.075, and 0.05, the amplitude-dependent hysteresis loops in the ϕ–i plane are as shown in Fig. 1(a). As can be observed, the area of the pinched hysteresis loop gradually shrinks as the excitation amplitude decreases. Similarly, the frequency-dependent hysteresis loops are illustrated in Fig. 1(b), obtained with the fixed amplitude $I_S = 0.1$ and varying excitation frequencies. One can see that the area of the pinched hysteresis loop gradually decreases as the excitation frequency increases. Furthermore, all hysteresis loops in Figs. 1(a) and 1(b) are pinched at and pass through the origin, confirming that the proposed element satisfies the fingerprints of an ideal meminductor: the pinched hysteresis loop and the zero-crossing property.

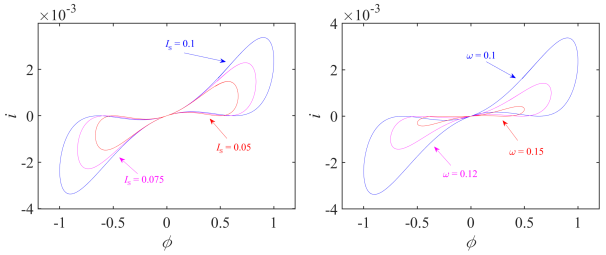


Fig. 1. Pinched hysteresis loops of the flux-controlled meminductor with parameters $a = 0$, $b = 0.2$, $k = 0.1$, $k_1 = 1$ and $k_2 = 1$. (a) Amplitude-dependent hysteresis loops with the fixed frequency $\omega = 0.1$. (b) Frequency-dependent hysteresis loops with the fixed amplitude $I_S = 0.1$.

2.2. Coupled HR–FHN model

The FHN neuron model is a widely used two-dimensional simplification capable of capturing essential neural excitability and spiking behaviors. Similarly, the two-dimensional HR model offers a reduction of the more complex Hodgkin–Huxley formalism. While isolated 2D HR or FHN neurons exhibit relatively simple dynamics, their coupling can lead to rich collective behavior. In this work, we couple a 2D HR neuron with a 2D FHN neuron via a meminductor in series with a linear resistor, as illustrated in Fig. 2. This topology provides a direct functional decomposition: the resistor models the fast, voltage-dependent ionic current that passes through postsynaptic channels, representing the instantaneous, dissipative aspect of synaptic transmission. The meminductor models the history-dependent, inductive aspect. Unlike a linear inductor, the meminductor's inductance is governed by its internal state variable, which integrates past neuronal activity (magnetic flux). This naturally captures the memory effect and state-dependent filtering akin to STP in biological synapses.

The governing equations of the coupled system are as follows:

$$\begin{cases} \dot{x}_1 = y_1 - a_1 x_1^3 + b_1 x_1^2 - k_m(a + b\rho^2)\varphi, \\ \dot{y}_1 = c_1 - d_1 x_1^2 - y_1, \\ \dot{x}_2 = x_2 - \frac{1}{3}x_2^3 - y_2 + k_m(a + b\rho^2)\varphi, \\ \dot{y}_2 = e(x_2 + a_2 - b_2 y_2), \\ \dot{\rho} = k\varphi - k_1\rho + k_2(x_1 - x_2 - (a + b\rho^2)\varphi R), \\ \dot{\varphi} = x_1 - x_2 - (a + b\rho^2)\varphi R, \end{cases} \tag{3}$$

where x_1 and x_2 represent the membrane potential variables of the HR neuron and the FHN neuron, respectively; y_1 and y_2 are the ion current variables of the two neurons. The parameters a_1, b_1, c_1, and d_1 are HR neuron parameters, while a_2, b_2, and e are parameters of the FHN neuron. The term k_m stands for the coupling strength. The parameter R represents the resistance in series with the meminductor. Note that the voltage across the meminductor synapse is expressed as $x_1 - x_2 - (a + b\rho^2)\varphi R$, and its current is expressed as $(a + b\rho^2)\varphi$.

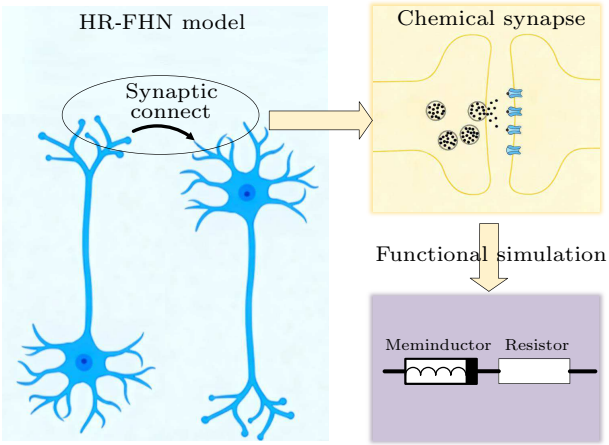


Fig. 2. Schematic of a 2D HR neuron and a 2D FHN neuron coupled by a series-connected meminductor and resistor. The resistor models the instantaneous synaptic conductance, while the meminductor (with state ρ) models the history-dependent plastic property, together functionally emulating a chemical synapse.

2.3. Equilibrium point analysis

Analyzing the equilibrium points and their stability is fundamental to understanding the long-term dynamics and possible attractors in the coupled neural network. The equilibrium points of the HR–FHN model are obtained by setting the time derivatives in Eq. (3) to zero, resulting in the following algebraic system:

$$\begin{cases} 0 = y_1 - a_1 x_1^3 + b_1 x_1^2 - k_{\mathrm{m}}(a + b\rho^2)\varphi, \\ 0 = c_1 - d_1 x_1^2 - y_1, \\ 0 = x_2 - \frac{1}{3}x_2^3 - y_2 + k_{\mathrm{m}}(a + b\rho^2)\varphi, \\ 0 = e(x_2 + a_2 - b_2 y_2), \\ 0 = k\varphi - k_1\rho + k_2(x_1 - x_2 - (a + b\rho^2)\varphi R), \\ 0 = x_1 - x_2 - (a + b\rho^2)\varphi R. \end{cases} \tag{4}$$

Finally, the relation between variables x_2 and ρ is given by

$$\begin{cases} F_1(x_2,\rho) = c_1 + (b_1 - d_1)(x_2 + \frac{k_1}{k}(a + b\rho^2)\rho R)^2 \\ \qquad\qquad - a_1(x_2 + \frac{k_1}{k}(a + b\rho^2)\rho R)^3 \\ \qquad\qquad - k_{\mathrm{m}}\frac{k_1}{k}(a + b\rho^2)\rho, \\ F_2(x_2,\rho) = (1 - \frac{1}{b_2})x_2 - \frac{1}{3}x_2^3 - \frac{1}{b_2}a_2 + k_{\mathrm{m}}\frac{k_1}{k}(a + b\rho^2)\rho. \end{cases} \tag{5}$$

Thus, the equilibrium points correspond to the intersection of the curves $F_1(x_2,\rho)$ and $F_2(x_2,\rho)$ in the x_2–ρ plane. As an illustrative example, the neuron parameters are fixed at $a_1 = 1$, $b_1 = 3$, $c_1 = 1$, $d_1 = 5$, $a_2 = 0.6$, and $b_2 = 0.1$, which correspond to commonly used parameter settings that enable typical spiking dynamics in HR and FHN neurons. The remaining parameters are set to $k = 0.1$, $k_1 = 1$, $R = 2$, $a = -0.2$, and $b = 0.2$, where a and b characterize the nonlinear meminductive response, and k and k_1 govern the evolution of the internal state variable of the meminductor. Under these conditions, the intersecting curves of $F_1(x_2,\rho)$ and $F_2(x_2,\rho)$ are plotted in Fig. 3 for two different coupling strengths: $k_{\mathrm{m}} = 0.2$ and $k_{\mathrm{m}} = 1.2$. The plots reveal multiple intersection points, indicating that the system possesses several equilibrium states whose number and location vary with k_{m}.

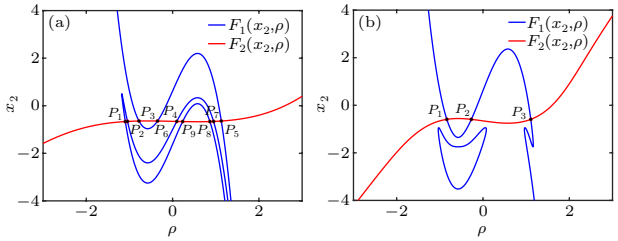


Fig. 3. Curves of $F_1(x_2,\rho)$ and $F_2(x_2,\rho)$: (a) $k_{\mathrm{m}} = 0.2$; (b) $k_{\mathrm{m}} = 1.2$. Intersections represent equilibrium points of the coupled system.

The local stability of each equilibrium point is determined by analyzing the eigenvalues of the Jacobian matrix J evaluated at that point. For the neural network model (4), the Jacobian is given by

$$J = \begin{bmatrix} -3a_1x_1^2 + 2b_1x_1 & 1 & 0 & 0 & -k_{\mathrm{m}}H_1 & -k_{\mathrm{m}}H_2 \\ -2d_1x_1 & -1 & 0 & 0 & 0 & 0 \\ 0 & 0 & 1 - x_2^2 & -1 & k_{\mathrm{m}}H_1 & k_{\mathrm{m}}H_2 \\ 0 & 0 & e & -eb_2 & 0 & 0 \\ k_2 & 0 & -k_2 & 0 & -k_1 - k_2RH_1 & k - k_2RH_2 \\ 1 & 0 & -1 & 0 & -RH_1 & -RH_2 \end{bmatrix}, \tag{6}$$

where $H_1 = 2b\rho\varphi$ and $H_2 = (a + b\rho^2)$. For the chosen parameter set, the computed eigenvalues for each equilibrium point (labeled P_1, P_2, …) are summarized in Table 1 for $k_{\mathrm{m}} = 0.2$ and Table 2 for $k_{\mathrm{m}} = 1.2$. In all cases, at least one eigenvalue possesses a positive real part, leading to the classification of every equilibrium as an unstable saddle focus (USF). The presence of such unstable equilibria, often accompanied by complex conjugate eigenvalue pairs, is a common indicator and necessary precondition for the emergence of chaotic dynamics in nonlinear systems.

Table 1. Stability analysis of equilibrium points when $k_{\mathrm{m}} = 0.2$ (USF: unstable saddle focus).

	(x_2,ρ)	Eigenvalues	Stability
P_1	$(-1.0956, -0.6655)$	-19.072; -18.413; 0.22724 ± 0.20969i; -0.059741; -0.053011	USF
P_2	$(-1.0444, -0.6602)$	-18.129; -10.776; 0.23046 ± 0.2036i; 0.078207; -0.049018	USF
P_3	$(-0.7787, -0.6432)$	-10.356; 0.70132 ± 1.7215i; 0.2468 ± 0.18821i; -0.031194	USF
P_4	$(0.0957, -0.6602)$	-10.568; -1.0985; 0.55322; 0.076041; 0.18089 ± 0.17133i	USF
P_5	$(1.1277, -0.6432)$	-21.226; 0.69396 ± 1.7223i; 0.24365 ± 0.19142i; -0.052598	USF
P_6	$(-0.3490, -0.6432)$	-2.6229; 0.72814 ± 1.7025i; 0.10332; 0.25987 ± 0.1487i	USF
P_7	$(0.9487, -0.6602)$	-14.917; -10.865; 0.23122 ± 0.20311i; 0.078277; -0.044101	USF
P_8	$(0.8637, -0.6655)$	-17.093; -12.956; 0.2292 ± 0.2082i; -0.060485; -0.039397	USF
P_9	$(0.2319, -0.6655)$	-17.346; -1.6563; -0.060886; 0.3312; 0.196 ± 0.14409i	USF

Table 2. Stability analysis of equilibrium points when $k_m = 1.2$ (USF: unstable saddle focus).

	(x_2, ρ)	Eigenvalues	Stability
P_1	$(-0.8376, 0.5923)$	-10.998; 0.13514 ± 1.576i; 0.1231 ± 0.31825i; -0.036952	USF
P_2	$(-0.2696, 0.59232)$	-1.6716; 0.41402 ± 1.4922i; 0.11865 ± 0.19513i; 0.40092	USF
P_3	$(1.1072, -0.5923)$	-19.52; 0.11284 ± 1.5559i; 0.11499 ± 0.32084i; -0.052008	USF

3. Dynamical characterization of the HR–FHN model

This section presents a systematic investigation of the nonlinear dynamics of the meminductor-coupled HR–FHN neural model. We focus on elucidating the effects of key parameters — specifically, the coupling strength k_m, coupling resistance R, and system initial conditions — on the electrical activity and synchronization behavior of the coupled neurons. For all subsequent analyses, the parameters of the HR neuron are set to $a_1 = 1$, $b_1 = 3$, $c_1 = 1$, and $d_1 = 5$, and those of the FHN neuron are set to $a_2 = 0.6$, $b_2 = 0.1$, and $e = 0.1$, corresponding to their intrinsic stable periodic firing regimes. The meminductor parameters are set to $a = -0.2$, $b = 0.2$, $k = 0.1$, $k_1 = 1$, and $k_2 = 1$. Numerical simulations are performed using the ODE45 algorithm with a time step of $\Delta t = 10^{-3}$, and the Lyapunov exponents (LEs) are calculated using the Wolf algorithm to quantitatively characterize the dynamical regimes.

3.1. Dynamics with respect to coupling strength k_m

We first examine the influence of the coupling strength k_m on the system's dynamics. The coupling resistance is fixed at $R = 1$, and the initial condition is configured as (0, 0, 0, 0, 0, 0). Figure 4(a) shows the bifurcation diagram of the membrane potential x_1 versus k_m, while Fig. 4(b) displays the corresponding spectrum of the first three largest LEs; the remaining three LEs are consistently negative and are thus omitted for clarity.

The system exhibits a rich repertoire of firing patterns as k_m varies. For weak coupling ($k_m < 0.6$), the system predominantly exhibits chaotic firing dynamics, indicated by the positive LE_1 in Fig. 4(b). As k_m increases into the interval $0.6 < k_m < 0.75$, the system undergoes a transition from chaotic to periodic firing, with LE_1 approximating zero. For medium coupling strengths ($0.75 < k_m < 1$), the system reenters a regime of chaotic oscillations. When the coupling strength becomes sufficiently large ($k_m > 1$), the system stabilizes into a periodic firing state characterized by near-zero LE_1.

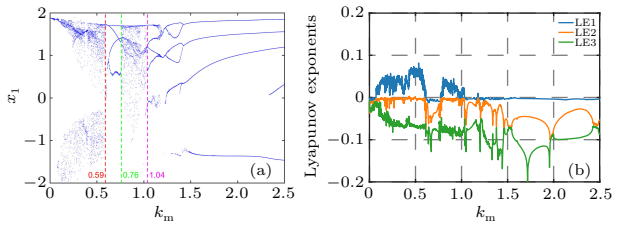


Fig. 4. Dynamics with respect to the coupling strength k_m: (a) bifurcation diagram; (b) LEs.

To intuitively illustrate these complex firing behaviors, representative phase diagrams in the y_1–x_1 plane and the corresponding time series of x_1 are shown in Fig. 5. When $k_m = 0.3$, the system exhibits chaotic firing, as illustrated in Figs. 5(a) and 5(b). At $k_m = 0.65$, the model demonstrates a period-four bursting pattern, as evident from Figs. 5(c) and 5(d). At $k_m = 1.3$, a period-six bursting pattern is observed, as illustrated in Figs. 5(e) and 5(f). Finally, at $k_m = 2.3$, the model exhibits a stable period-three bursting pattern, as shown in Figs. 5(g) and 5(h). These results confirm that k_m serves as an effective bifurcation parameter, capable of inducing transitions between bursting and chaotic firing states.

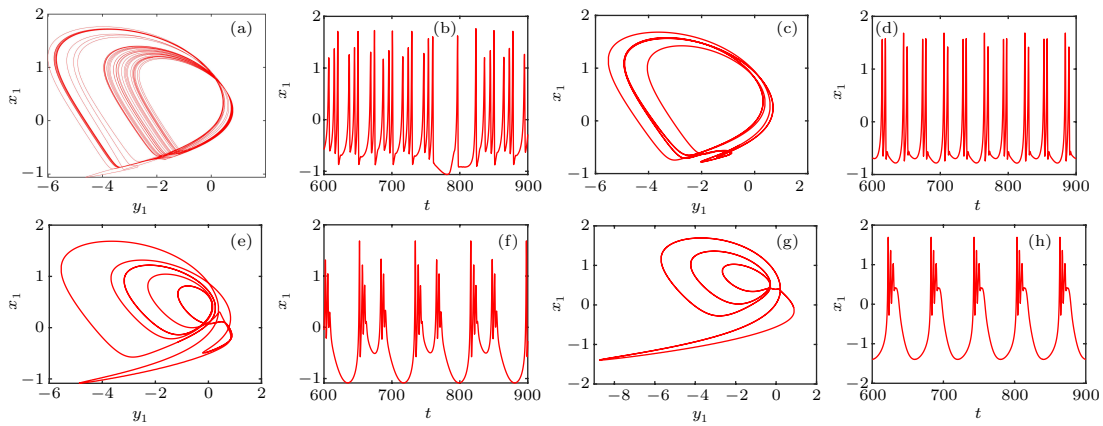


Fig. 5. Phase diagrams in the y_1–x_1 plane and time sequence diagrams of state x_1: (a) and (b) chaotic firing at $k_m = 0.3$; (c) and (d) period-four bursting at $k_m = 0.65$; (e) and (f) period-six bursting at $k_m = 1.3$, (g) and (h) period-three bursting at $k_m = 2.3$.

3.2. Dynamics with respect to R

Next, we analyze the role of the coupling resistance R in shaping the system's dynamics. The coupling strength is fixed at $k_{\mathrm{m}} = 1.1$, with the initial condition remaining at (0, 0, 0, 0, 0, 0). The corresponding bifurcation diagram and LEs are shown in Figs. 6(a) and 6(b), respectively. From Fig. 6(a), it can be observed that the model initially exhibits chaotic firing within the range $R \in (0, 0.5)$. In the wider parameter range $R \in [0.5, 1.43)$, the model exhibits alternating periodic and chaotic firing behaviors, with multiple chaotic windows embedded within periodic regions — a hallmark of complex nonlinear dynamics. At $R = 1.43$, the model transitions from chaotic firing back to periodic firing, subsequently stabilizing into a periodic firing state for $R > 1.43$. The LEs shown in Fig. 6(b) quantitatively confirm these transitions, with positive exponents corresponding to chaotic regimes and near-zero exponents indicating periodic behavior.

To provide an intuitive illustration, selected phase diagrams and time sequences corresponding to different values of R are depicted in Fig. 7. When $R = 0.2$, the neuron exhibits chaotic firing, as shown in Figs. 7(a) and 7(b). At $R = 0.7$, the neuron transitions into a period-four bursting state, as illustrated in Figs. 7(c) and 7(d). When $R = 1.1$, the neuron shifts back to chaotic firing, as demonstrated in Figs. 7(e) and 7(f). Subsequently, a period-three bursting pattern is observed at $R = 1.6$, as shown in Figs. 7(g) and 7(h).

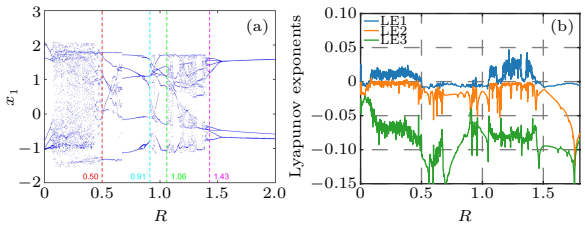


Fig. 6. Dynamics with respect to the coupling resistance R: (a) bifurcation diagram; (b) LEs.

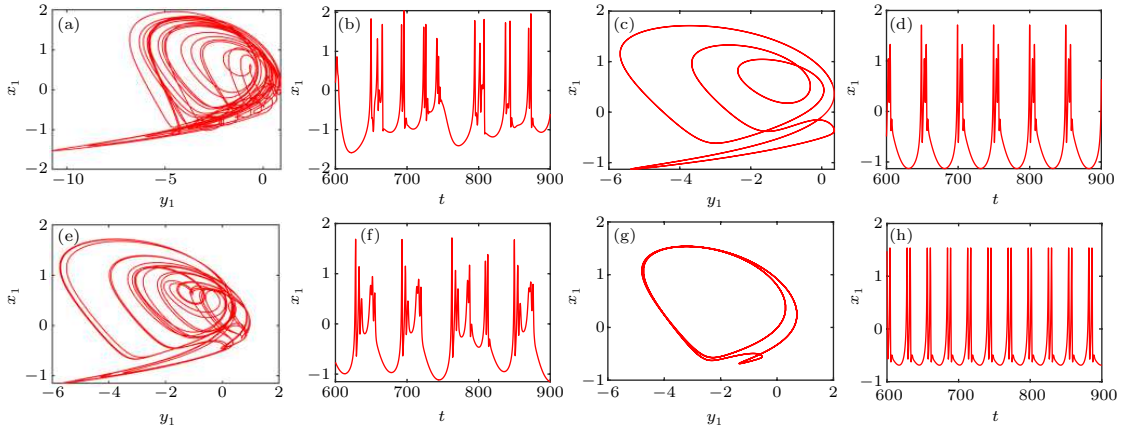


Fig. 7. Phase diagrams in the y_1–x_1 plane and time sequence diagrams of state x_1: (a) and (b) chaotic firing at $R = 0.2$; (c) and (d) period-four bursting at $R = 0.7$; (e) and (f) chaotic firing at $R = 1.1$, (g) and (h) period-three bursting at $R = 1.6$.

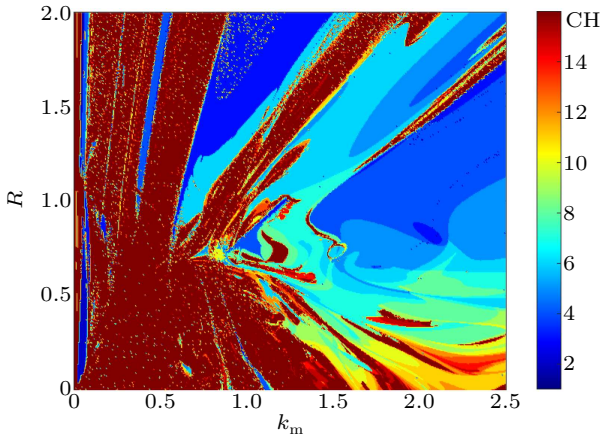


Fig. 8. Dynamical map with respect to the control bifurcation parameters k_{m} and R. Colors indicate firing periods (1–14), with "CH" denoting chaotic regimes.

As mentioned above, independently varying the control parameters k_{m} and R can induce a wide array of firing dynamics. To gain a global perspective on the system's behavior, we construct a two-parameter dynamical map, a powerful tool for visualizing the global dynamics of nonlinear systems. Keeping the initial conditions at (0, 0, 0, 0, 0, 0), we vary $k_{\mathrm{m}} \in [0, 2.5]$ and $R \in [0, 2]$. The resulting dynamical map is shown in Fig. 8.

In this map, different colors represent distinct firing periods, labeled from "1" (period one) to "14" (period fourteen). Regions colored in red and marked "CH" indicate chaotic firing, operationally defined here as a firing period greater than 14. The map clearly illustrates that both k_{m} and R play crucial and interconnected roles in determining the firing patterns of the coupled neuron system, revealing complex boundaries between periodic and chaotic regimes.

3.3. Dynamics with respect to the initial conditions

Multistability — the coexistence of multiple stable firing states under identical system parameters but different initial conditions — is a hallmark of neuronal systems. This phe-

nomenon is critical for diverse brain functions such as memory formation and decision-making, and it also holds significant implications for neuromorphic computing.

To investigate the initial-condition-dependent coexisting firing dynamics, the system parameters are fixed at $k_2 = 2$, $k_m = 0.2$, and $R = 1.5$, and the initial condition is set to $(0,0,0,0,\rho(0),0)$, where $\rho(0)$ serves as the bifurcation parameter. The resulting bifurcation diagram of x_1 and the corresponding finite-time LEs are shown in Figs. 9(a) and 9(b), respectively. The complex dependence of the firing pattern on $\rho(0)$ is evident, with alternating windows of periodic and chaotic behavior.

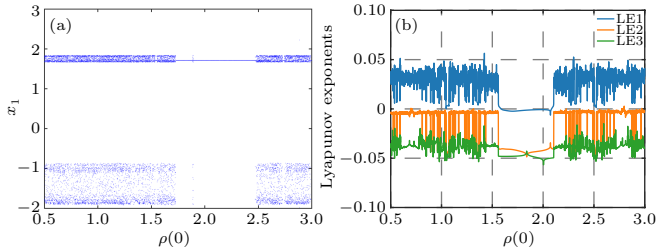


Fig. 9. Dynamics with respect to the initial condition $\rho(0)$: (a) bifurcation diagram, (b) LEs.

The attractor basin is used to describe the distribution of attractors and the possible number of categories in the space of initial conditions. Keeping the system parameters constant, we vary the initial values of the meminductor state $\rho(0)$ and flux $\phi(0)$ within the ranges $[0,3]$, while keeping the other initial values at zero. The resulting local basin of attraction in the $\rho(0)$–$\phi(0)$ plane is shown in Fig. 10, clearly illustrating the distribution of basins corresponding to different attractors.

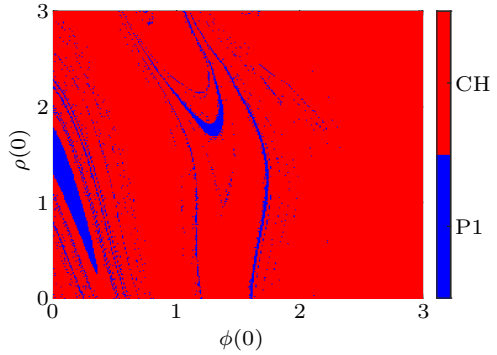


Fig. 10. Attraction basin of the $\varphi(0)$–$\rho(0)$ plane. Different colors correspond to distinct asymptotic firing patterns.

To further illustrate this multistability, we select two specific initial values for the meminductor: $\rho(0) = 1$ and $\rho(0) = 2$. The corresponding time series and phase portraits are plotted in Fig. 11. Different colors represent distinct firing modes: red denotes a chaotic firing pattern, while blue represents a period-one pattern. These results confirm that the firing pattern of the neuron can be effectively regulated by the initial state of the meminductor, showcasing a clear and robust case of activity-dependent multistability — directly demonstrating the memory-driven plasticity of our proposed synaptic model.

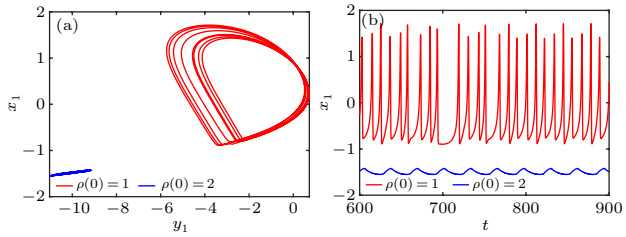


Fig. 11. Multistability with respect to the initial condition $\rho(0)$: (a) phase diagram in the y_1–x_1 plane; (b) time series of x_1.

3.4. Phase synchronization

In heterogeneous coupled neuron networks, complete synchronization is typically difficult to achieve. Therefore, phase synchronization is a more relevant and practical measure of coordinated activity. The burst phase is defined as[33,34]

$$\theta(t) = 2n\pi + 2\pi\frac{t - t_n}{t_{n+1} - t_n}, \quad (t_n \le t \le t_{n+1}), \tag{7}$$

where t_n is the onset time of the n-th burst, and $t_{n+1} - t_n$ denotes the burst interval. Phase synchronization can be discerned by detecting the phase difference between two neurons, as follows:

$$|\Delta\theta(t)| = |\theta_1(t) - \theta_2(t)|. \tag{8}$$

Here, the absolute value ensures a positive phase difference. Phase synchronization is considered to be achieved when $\Delta\theta(t)$ converges to a constant or oscillates within a small bounded range.

We first analyze the phase difference over the time interval $[0,1000]$ for different coupling strengths k_m, while keeping the other parameters and initial conditions consistent with those in Subsection 3.1. The results are shown in Fig. 12, where the blue and red curves correspond to HR and FHN neurons, respectively. When the coupling strength between the two neurons is zero, the phase difference increases linearly over time, indicating independent, free-running firing of the two neurons, as shown in Figs. 12(a) and 12(b). For $k_m = 2$, the phase difference continues to increase without converging, signifying that the two neurons remain out of synchronization, as shown in Figs. 12(c) and 12(d). When k_m is increased to 4, the phase difference fluctuates within a narrow bound $[0,0.6]$, indicating the emergence of phase synchronization between the two neurons, as illustrated in Figs. 12(e) and 12(f). At a strong coupling of $k_m = 10$, the phase difference remains minimal, stabilizing around 0.2, suggesting that the coupled neurons are nearly in complete synchronization, as shown in Figs. 12(g) and 12(h).

Notably, the coupling resistance R also plays a critical role in synchronization. With k_m fixed at 2, a coupling resistance $R = 2$ results in significant fluctuations in the phase difference, indicating a pronounced desynchronization state, as shown in Figs. 13(a) and 13(d). In contrast, a small resistance

($R = 0.1$) causes the phase difference to converge, facilitating the onset of phase synchronization, as shown in Figs. 13(b) and 13(e). When $R = 0$, the dissipative component disappears and the coupling is dominated by the meminductor. Since the meminductor primarily introduces memory modulation rather than dissipation, this leads to desynchronization, as shown in Figs. 13(c) and 13(f). These results confirm that the coupling resistance R (the instantaneous pathway) and the meminductive state (the plastic pathway) provide two independent yet interactive control knobs for tuning network synchrony. This dual-parameter control mimics the multifaceted regulation of signal integration observed in real neural systems.

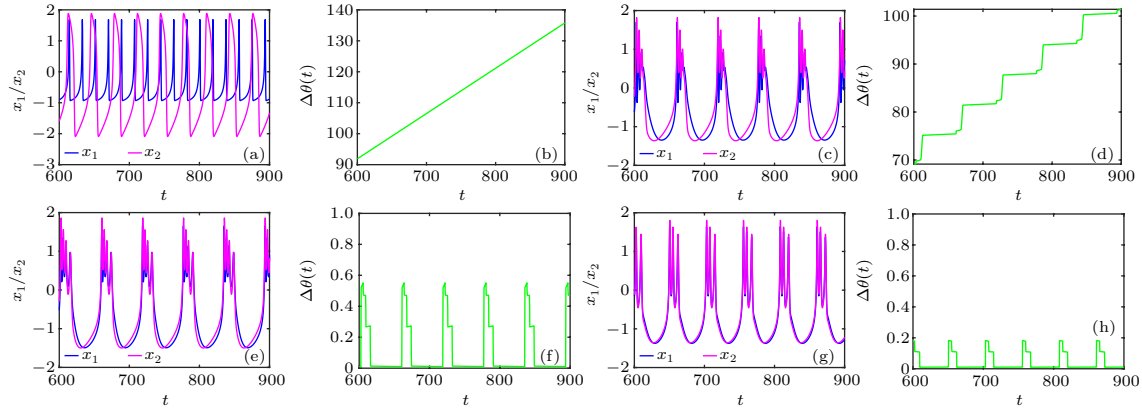


Fig. 12. Time series and phase differences at different coupling strengths: (a) and (b) $k_m = 0$; (c) and (d) $k_m = 2$; (e) and (f) $k_m = 4$, (g) and (h) $k_m = 10$.

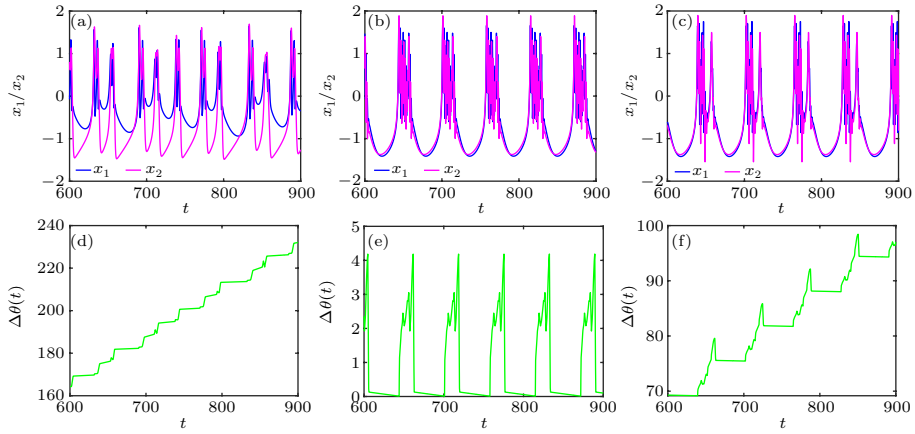


Fig. 13. Time series and phase differences at different coupling resistances with a fixed coupling strength $k_m = 2$: (a) and (d) $R = 2$; (b) and (e) $R = 0.1$; (c) and (f) $R = 0$.

4. DSP implementation of the coupled HR–FHN model

To verify the feasibility and operational stability of the proposed meminductor-coupled heterogeneous neural system in practical hardware environments, the model is extended from numerical simulation to a real-time digital hardware platform. Digital signal processing (DSP) systems, owing to their strong real-time floating-point computation capability and excellent numerical stability, have been widely adopted for hardware implementations of chaotic systems and neural dynamical models.[35,36] Furthermore, the memory-dependent coupling characteristic of the meminductor may offer additional flexibility for real-time modulation and adaptive synchronization control.[37]

In this work, a coupled HR–FHN model is implemented on a DSP platform whose architecture is depicted in the block diagram of Fig. 14. The system is centered around a 32-bit floating-point DSP chip (TMS320F28335), which executes the system of differential equations (Eq. (4)) in real time. The computed state variables are then converted into analog voltages via a dual-channel, 16-bit digital-to-analog converter (DAC8552), enabling direct visualization of dynamic attractors via a digital oscilloscope (Tektronix MSO 3032). Communication between the host computer and the DSP board is established via a TI XDS100v1 USB emulator, allowing the algorithm to be uploaded and real-time debugging to occur within the Code Composer Studio (CCS) integrated development environment.

Prior to loading the computational algorithm onto the DSP, essential initialization procedures are performed, including configuring the system clock, initializing the DAC, setting up timer interrupts for precise numerical integration, and al-

locating memory for state variables and parameters. The numerical integration algorithm implemented on the DSP is the fourth-order Runge–Kutta (RK4) method, chosen for its well-balanced trade-off between computational accuracy and execution speed, making it suitable for real-time operation. The integration step size is set to $h = 0.001$, which is consistent with the numerical simulations. In addition, the sampling frequency and numerical precision of the DSP platform are sufficiently high that quantization errors have a negligible influence on the dynamical behavior.

The physical hardware setup is shown in Fig. 15. To match the voltage output range of the DSP platform (confined to -5 V to $+5$ V), the original state variables are linearly scaled before being sent to the DAC. Consequently, the phase portraits captured on the oscilloscope correspond to these scaled signals, with each grid division representing 2 V in accordance with the oscilloscope settings.

The experimentally measured phase portraits in the y_1–x_1 plane are displayed in Figs. 16 and 17, corresponding to different values of the coupling strength k_m and the coupling resistance R, respectively. A direct comparison between these hardware results and the software simulations presented in Section 3 (Figs. 5 and 7) reveals a close qualitative and quantitative agreement. The DSP implementation successfully reproduces all major firing patterns — including chaotic spiking, period-four bursting, period-six bursting, and period-three bursting — across the tested parameter ranges. This strong correspondence between numerical simulation and experimental measurement confirms both the correctness of the digital implementation algorithm and the physical realizability of the proposed meminductor-coupled HR–FHN neuron system.

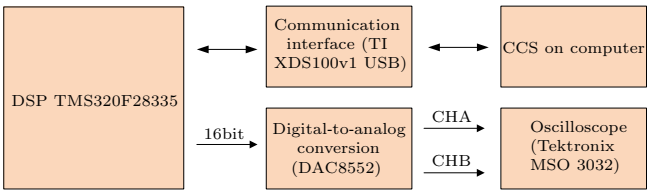


Fig. 14. Block diagram of the DSP hardware implementation.

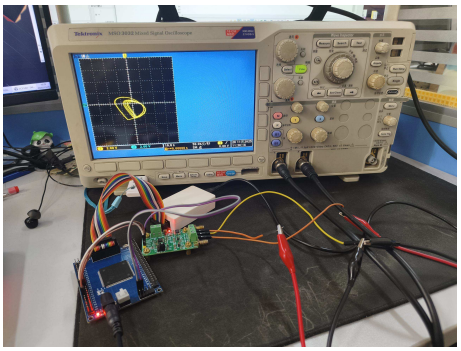


Fig. 15. Photograph of the DSP-based experimental platform.

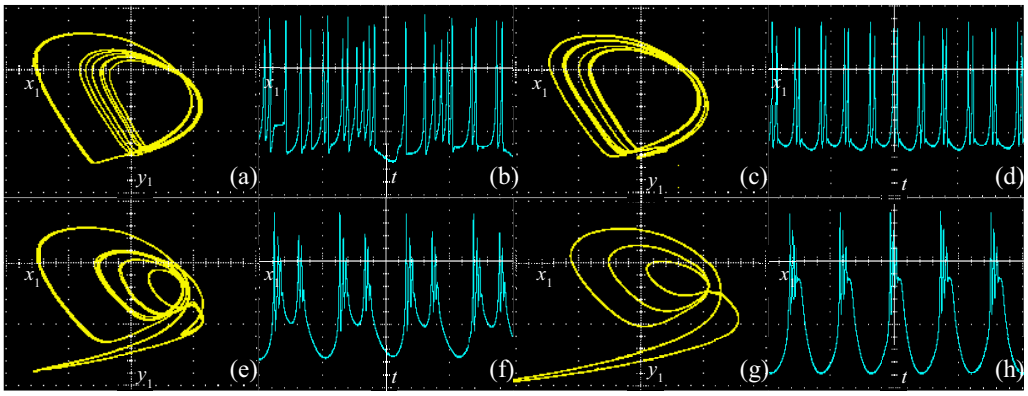


Fig. 16. Experimentally measured phase portraits (left column) and time series (right column) in the y_1–x_1 plane for $R = 1$ at different values of k_m: (a) and (b) $k_\mathrm{m} = 0.3$; (c) and (d) $k_\mathrm{m} = 0.65$; (e) and (f) $k_\mathrm{m} = 1.3$; (g) and (h) $k_\mathrm{m} = 2.3$.

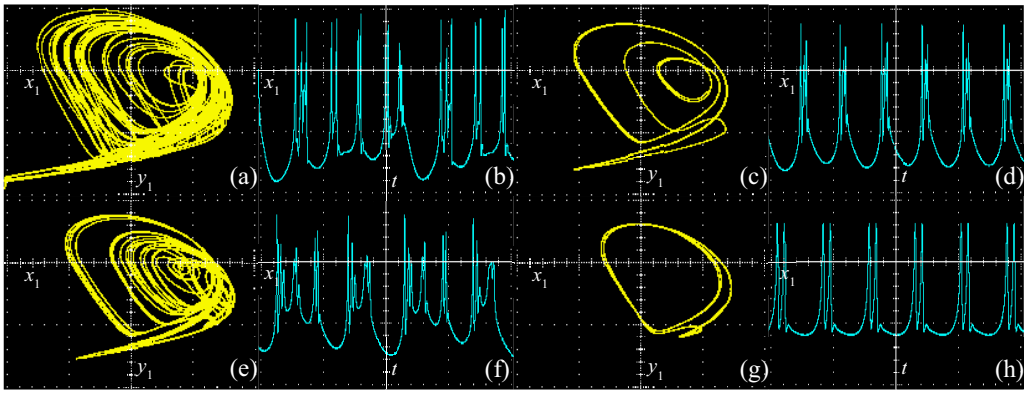


Fig. 17. Experimentally measured phase portraits (left column) and time series (right column) in the y_1–x_1 plane for $k_\mathrm{m} = 1.1$ at different values of R: (a) and (b) $R = 0.2$; (c) and (d) $R = 0.7$; (e) and (f) $R = 1.1$; (g) and (h) $R = 1.6$.

In summary, the successful DSP-based realization of the model not only verifies its feasibility in practical digital hardware but also highlights the potential of meminductor-based synaptic architectures for future neuromorphic computing applications where real-time, reconfigurable, and biologically plausible neural dynamics are required.

5. Conclusion

This study presents a heterogeneous neural network architecture interconnected via a meminductor-resistor series synapse, enabling a functional decomposition of chemical synaptic transmission. The linear resistor models instantaneous signal conduction, whereas the meminductor emulates history-dependent plasticity through its state-dependent inductance characteristics. A systematic investigation reveals that the coupled system exhibits rich dynamical behaviors governed by two key parameters: the coupling strength k_{m} and the coupling resistance R. Through bifurcation analysis and LE calculations, we demonstrate that these parameters independently regulate transitions among chaotic spiking, periodic bursting, and complex alternations between periodic and chaotic dynamics. The two-parameter dynamical map further elucidates the intricate interplay between these control variables and the resulting firing patterns. The meminductive synapse introduces activity-dependent multistability, wherein different initial conditions lead to coexisting attractors with distinct firing characteristics. This property closely resembles the STP observed in biological synapses and provides a mechanism for history-dependent signal processing. Phase synchronization analysis indicates that the coupling resistance R enables independent modulation of neural coordination, complementing the influence of coupling strength (k_{m}). Experimental validation on a DSP platform confirms the physical realizability of the proposed architecture. The close agreement between hardware measurements and numerical simulations underscores the model's feasibility for implementation in practical digital systems. This work establishes a functionally decomposed synaptic model that bridges theoretical analysis with hardware realization, offering a versatile platform for investigating meminductor-based neural systems with potential applications in neuromorphic computing and adaptive information processing.

Acknowledgments

Project supported by the National Natural Science Foundations of China (Grant No. 62171401) and the Key Research Project of the Hunan Provincial Department of Education (Grant No. 25A0146).

References

[1] Chua L 1971 *IEEE Trans. Circuit Theory* **18** 507
[2] Strukov D B, Snider G S, Stewart D R, *et al.* 2008 *Nature* **453** 80
[3] Tour J M and He T 2008 *Nature* **453** 42
[4] Di Ventra M, Pershin Y V and Chua L O 2009 *Proc. IEEE* **97** 1717
[5] Duan L, Lu Q and Wang Q 2008 *Neurocomputing* **72** 341
[6] Ma J 2023 *J. Zhejiang Univ. Sci. A* **24** 109
[7] Hu B, Guan Z H, Chen G, *et al.* 2021 *IEEE Trans. Cybern.* **52** 10214
[8] Mou J, Ma T, Banerjee S, *et al.* 2024 *IEEE Trans. Circuits Syst. I Regul. Pap.* **71** 1771
[9] Pereda A E 2014 *Nat. Rev. Neurosci.* **15** 250
[10] Yao Z, Sun K and He S 2023 *Nonlinear Dyn.* **111** 19411
[11] Tian H, Wang J, Ma J, *et al.* 2025 *Chaos Solitons Fractals* **199** 116863
[12] Xu F, Zhang J, Fang T, *et al.* 2018 *Nonlinear Dyn.* **92** 1395
[13] Serb A, Corna A, George R, *et al.* 2020 *Sci. Rep.* **10** 2590
[14] Qin M, Lai Q, Wang H, *et al.* 2025 *Chaos* **35** 023123
[15] Boya B F B A, Babenko L K, Rangel-Magdaleno J D J, *et al.* 2025 *Neural Netw.* **196** 108333
[16] Yang F, Song X and Yu Z 2024 *Chaos Solitons Fractals* **188** 115496
[17] Yu H, Wang J, Du J, *et al.* 2015 *Cogn. Neurodyn.* **9** 93
[18] Anderson P A 1985 *J. Neurophysiol.* **53** 821
[19] Yao Z, Wang C, Zhou P, *et al.* 2021 *Commun. Nonlinear Sci. Numer. Simul.* **95** 105583
[20] Liu Z, Zhou S, Zhu R, *et al.* 2025 *Chaos Solitons Fractals* **191** 115918
[21] Li Z, Xue W, Xu Q, *et al.* 2025 *Chaos Solitons Fractals* **197** 116545
[22] Yao Z, Ma J, Yao Y, *et al.* 2019 *Nonlinear Dyn.* **96** 205
[23] Wu F, Guo Y and Ma J 2022 *Nonlinear Dyn.* **109** 2063
[24] Yao Z, Sun K and He S 2023 *Nonlinear Dyn.* **111** 19411
[25] Chen S, Zhang T, Tappertzhofen S, *et al.* 2023 *Adv. Mater.* **35** 2301924
[26] Lee Y and Lee T W 2019 *Acc. Chem. Res.* **52** 964
[27] Wang F Z 2023 *Micromachines* **14** 486
[28] Dinavahi A, Yamamoto A and Harris H R 2023 *Sci. Rep.* **13** 1817
[29] Li C, Zhang X, Chen P, *et al.* 2023 *iScience* **26** 106315
[30] Zhang J, Yang L, Zuo J, *et al.* 2025 *Chaos Solitons Fractals* **199** 116662
[31] Ding X, Fan W, Wang N, *et al.* 2025 *Chaos Solitons Fractals* **199** 116658
[32] Shi F, Cao Y, Banerjee S, *et al.* 2024 *Chaos Solitons Fractals* **189** 115723
[33] Yan X, Li Z and Li C 2024 *Chin. Phys. B* **33** 028705
[34] Ma M, Xiong K, Li Z, *et al.* 2024 *Chin. Phys. B* **33** 028706
[35] Mou J, Cao H, Zhou N, *et al.* 2024 *IEEE Trans. Cybern.* **54** 7333
[36] Cao H, Wang Y, Banerjee S, *et al.* 2024 *Chaos Solitons Fractals* **179** 114466
[37] Ding D, Niu Y, Zhan H, *et al.* 2024 *Chin. Phys. B* **33** 050503